Submitted to the Journal of Applied Physics,

Assigned manuscript #JR-9871

December 20, 2011

Plasma potential mapping of high power impulse magnetron sputtering discharges

Albert Rauch,[1] Rueben J. Mendelsberg,[1] Jason M. Sanders,[1,2] and André Anders[1,*]

[1]*Lawrence Berkeley National Laboratory, University of California, Berkeley, California 94720, USA*

[2]*on leave from the Department of Electrical Engineering, University of Southern California, Los Angeles, California 90089, USA*

**Corresponding author: aanders@lbl.gov*

ACKNOWLEDGMENT

We thank J. Wallig for technical support. A.R. thanks the Austrian Marshall Plan Foundation (www.marshallplan.at) for funding a scholarship. A.A. acknowledges support by the Assistant Secretary for Energy Efficiency and Renewable Energy, Office of Building Technology of the U.S. Department of Energy. This work was done at Lawrence Berkeley National Laboratory with support by the U.S. Department of Energy under Contract No. DE-AC02-05CH11231.

Plasma potential mapping of high power impulse magnetron sputtering discharges

Albert Rauch,[1] Rueben J. Mendelsberg,[1] Jason M. Sanders,[1,2] and André Anders[1,*]

[1]*Lawrence Berkeley National Laboratory, University of California, Berkeley, California 94720, USA*

[2]*on leave from the Department of Electrical Engineering, University of Southern California, Los Angeles, California 90089, USA*

**Corresponding author: aanders@lbl.gov*

Abstract

Pulsed emissive probe techniques have been used to determine the plasma potential distribution of high power impulse magnetron sputtering (HiPIMS) discharges. An unbalanced magnetron with a niobium target in argon was investigated for pulse length of 100 μs at a pulse repetition rate of 100 Hz, giving a peak current of 170 A. The probe data were taken with a time resolution of 20 ns and a spatial resolution of 1 mm. It is shown that the local plasma potential varies greatly in space and time. The lowest potential was found over the target's racetrack, gradually reaching anode potential (ground) several centimeters away from the target. The magnetic pre-sheath exhibits a funnel-shaped plasma potential resulting in an electric field which accelerates ions toward the racetrack. In certain regions and times, the potential exhibits weak local maxima which allow for ion acceleration to the substrate. Knowledge of the local **E** and static **B** fields lets us derive the electrons' $\mathbf{E} \times \mathbf{B}$ drift velocity, which is about 10^5 m/s and shows structures in space and time.

PACS numbers: 52.25.-b, 52.25.Jm, 52.70.Ds, 52.80.Sm

I. INTRODUCTION

High Power Impulse Magnetron Sputtering (HiPIMS) is an increasingly popular ionized physical vapor deposition (i-PVD) technology that combines magnetron sputtering with pulsed power technology.[1-3] In contrast to conventional magnetron sputtering it provides greater opportunity to engineer the microstructure and improve the quality of thin films by utilizing the kinetic and potential energies of ions of the target material.[4-6]

In HiPIMS, high power pulses with typical lengths of 50-500 μs are applied to a conventional magnetron. To keep the average power within the specifications of the magnetron, the HiPIMS process is done with a low duty cycle and repetition rates less than 1 kHz. Special power supplies are available today from several vendors; they feature high peak currents and fast arc suppression circuits. The power density, averaged over the target area, can reach, and occasionally even exceed, 10^7 W/m². As a result, plasma densities of order 10^{19} m^{-3} in front of the target are not uncommon.[7,8] Sputtered atoms traveling from the target surface and passing through the dense plasma are likely ionized and thus participate in the sputtering process; such self-sputtering is characteristic for HiPIMS.[9-12] In addition to self-sputtering, gas atoms may be repeatedly ionized in the plasma and neutralized at the target surface, i.e. gas "recycling" (ionization-neutralization-ionization) can be an important process working in parallel to self-sputtering.[13]

Magnetrons are characterized by a closed-drift of electrons: the large azimuthal Hall current, primarily caused by the $\mathbf{E}\times\mathbf{B}$ drift of electrons, exceeds the discharge current by a factor of 3-9 for direct current (dc) conditions.[14] This factor is smaller for HiPIMS conditions,[15] which can be associated with "anomalous" current transport across magnetic field lines based on collective processes (oscillations and instabilities). Non-uniformities of the electric and magnetic fields give rise to additional electron drifts, including $\nabla B\times\mathbf{B}$ and higher order drifts. Lundin *et al.* suggested that the anomalous electron transport is caused by fast (MHz) oscillations in the electric field in the azimuthal direction based on dual-probe observations.[16] HiPIMS plasmas contain counter-streaming fluxes of ions, electrons and neutrals, all in the presence of a magnetic field, and therefore one should expect a whole variety of waves and instabilities.[17] In a recent paper we imaged dense plasma zones that move along the racetrack.[18] Through combined end-on and side-on imaging it was shown that each location of a strong plasma density gradient along the racetrack is associated with the formation of an electron jet and plasma protuberance moving away from the target.

The explanation of these phenomena is closely related to the knowledge of the local electric and magnetic fields. In this work, we first map the static magnetic field in the absence of plasma. Then we measure the electric field evolution during HIPIMS pulses with good time and spatial resolution in order to gain a deeper understanding of the HiPIMS discharge. For the present work we picked a relatively simple situation, namely HiPIMS discharges with constant-voltage pulses using a niobium target operating in a noble gas (argon). We will show time-resolved local data of the plasma potential, and proceed to collecting several 10^9 data points from about 10^6 individual HiPIMS pulses, which allows us to construct potential and electric field distributions averaged over 100 pulses per location. Such data are helpful in interpreting features of HiPIMS, including the moving dense plasma zones and electron jet formation.

II. EMISSIVE PROBE TECHNIQUES

Before we go into the details of the experiments and results, we very briefly recap plasma probe techniques, and in particular emissive probe techniques, as applied to HiPIMS discharges. Not surprisingly, HiPIMS plasma has been extensively studied using Langmuir probes.[19-23] Various levels of time resolution have been demonstrated for selected positions of the probe, mostly focusing on the interesting region above the racetrack. However, measurements generally lack the survey character that may allow us to gain greater insights.

Langmuir probes are a standard diagnostic for making density and temperature measurements in plasmas.[24,25] In principle, the plasma potential V_p can be determined using a conventional (cold) Langmuir probe via

$$V_p = V_f + \frac{kT_e}{e\,\overline{Q}} \ln\left(\frac{I_{es}}{I_{is}}\right) \tag{1}$$

where V_f is the floating potential (the potential of the probe when the probe current is zero), T_e is the electron temperature, k is the Boltzmann constant, e is the elementary charge, $\overline{Q}$ is the mean charge state number of ions arriving at the probe (in most cases, $\overline{Q}=1$ is a reasonable assumption); I_{es} and I_{is} are the electron and ion saturation currents, respectively. It is clear from Eq. (1) that this technique requires knowledge of the electron temperature and the saturation currents, which in principle can be taken from the probe characteristic. However that is not always simple since small probes do not show electron saturation due to the voltage dependence of the probe's sheath size, i.e. its effective collecting area. Furthermore, relation (1) was derived assuming that the plasma electrons have a Maxwell distribution, which is not the case in $\mathbf{E}\times\mathbf{B}$ discharges. Additionally, the approach inherently has great errors whenever the plasma is not quiescent. In strongly fluctuating plasmas, it is difficult to accurately observe the knee in the current-voltage characteristic that indicates the onset of electron saturation. Therefore it may be impossible to obtain satisfactory values for the plasma potential using a cold probe.

Emissive probes are superior and widely used when it comes to the determination of the plasma potential.[26-35] As the name suggests, an emissive probe is sufficiently hot to emit electrons via the thermionic emission mechanism, where the current density is approximately described by the Richardson-Dushman equation (*cf.* e.g. chapter 3 of ref.[36])

$$j_{thermionic} = A_R C_R T^2 \exp\left(-\frac{\phi}{kT}\right), \tag{2}$$

where $A_R = 4\pi e m_e k^2/h^3 = 1.202\times10^6$ A/m^{2}K^2 is the universal Richardson constant, C_R is a material-specific correction factor (0.5 for tungsten),[37] and ϕ is the work function of the metal (about 4.5 eV for tungsten).[37] The emitted electrons cause an additional current if the probe potential is equal to or lower than the potential of the surrounding plasma, otherwise they return to the probe. Therefore, the probe current for the emissive probe diverges from the current of a collecting-only probe when the bias voltage is less than the plasma potential. Therefore, one obvious way of determining the plasma potential is to find the potential where the emissive (hot) and collecting-only (cold) probe characteristics merge.[34]

When the emitted electron current of the probe is increased by increasing the probe's heating current, the probe's floating potential shifts toward the plasma potential. This becomes

clear when considering a generalization of Eq. (1) for the emissive probe by appropriately adding the emitted electron current I_{em} to the current balance (emitted electrons are electrically equivalent to collected ions):[38]

$$V_p = V_f + \frac{kT_e}{eQ} \ln\left(\frac{I_{es}}{I_{is} + I_{em}} \right). \quad (3)$$

Eq. (3) shows that for increasing emitter temperature, I_{em} increases (*cf.* Richardson-Dushman equation (2)) and thus the second term in (3) decreases. The floating potential V_f of the probe approaches V_p. The second term vanishes for $I_{em} = I_{es} - I_{is}$. If the probe temperature and thus the emission current is further increased, emitted electrons will be reflected by the plasma and return to the probe, keeping the probe at the plasma potential.[39] The plasma potential can therefore be obtained from the floating potential of the emissive probe once it is known that the emission current is sufficiently high. We will later show that this is the case for our setup, and we also will illustrate a case when probe heating did not lead to sufficient emission.

The floating emissive probe follows the fast changes in plasma potentials. A potential can readily be recorded with high time resolution (e.g. corresponding to a bandwidth of ~ 100 MHz or better) using a suitable high performance digital oscilloscope. The space resolution is limited by the size of the probe including its sheath; a resolution of 1 mm has been demonstrated.[40] Emissive probes have been successfully applied to measure plasma potentials in a wide range of magnetic fields, from tens of mT for a quadrupole device[41] to 0.5 T at the edge of a Tokamak[38] or *Q*-machine.[42]

It should be noted that the emitted electrons have energies of about 0.3 eV, corresponding to a wire temperature of $T_w \approx 3000$ K. This limits the voltage resolution of the emissive probe to about 0.3 V, which is generally not of concern given the errors of the potential measurements resulting from other factors. Among those factors is the presence of an ohmic voltage drop associated with the heating current of the probe's wire loop or filament. This voltage drop is undesirably high, typically a few volts.[42] That is, one side of the filament has a potential a few volts higher than the other side. In our previous work we have introduced a pulsed version of an emissive probe that addresses this issue by alternating between heating and measuring intervals.[43] The voltage driving the heating current is only applied in the pause between measurements, and the probe remains sufficiently hot for electron emission when the measurement is done. Our previous work[43] offers further details of the pulsed probe's circuitry and a discussion on emissive probe principles. Here we present extensive measurements related to the potential of HiPIMS plasmas using a niobium target in argon.

III. EXPERIMENTAL DETAILS

The experimental setup and the region of probe measurements are schematically presented in Fig. 1. A stainless steel vacuum chamber of 35 cm inner diameter and 25 cm inner height was pumped with a 550 l/s turbomolecular pump (Pfeiffer TMH 521, backed by a diaphragm pump) to a base pressure of about 10^{-5} Pa. High purity argon was introduced by a mass flow controller (MKS, maximum flow 100 sccm). Throughout all experiments, the argon flow rate was kept at 36 sccm. The combination of flow and pumping speed gave a pressure of 0.26 Pa as recorded by a capacitance manometer (Baratron by MKS).

The planar magnetron (US Inc., now MeiVac Inc.) was operated with a 6.25 mm (1/4") thick, 76 mm (3") diameter niobium target surrounded by a grounded anode ring mounted flush with the target surface. No target clamp ring is needed thanks to the magnetic target mount. The probe tip can therefore scan the whole target area without mechanical interference. The magnet assembly of the magnetron consists of a central cylinder magnet and an outer ring magnet located under the powered target electrode. This setup is typical for the required dome-shape of the magnetic field, leading to a ring-like dense plasma region whose projection onto the target surface produces the "racetrack," i.e. the zone of strongest sputtering. Due to the axial symmetry of the setup including the magnetron's magnetic field, the probe position and probe data can be described using cylindrical (*r,z*) coordinates. The magnetic field strengths in axial and radial directions, B_z and B_r respectively, were measured with an accuracy of about 1% using a small Hall probe (F.W. Bell 5180 Gaussmeter). The probe tip was mounted on the same movable arm that was later used for the emissive probe motion. The magnetic field was measured in the absence of the discharge, i.e. changes of the magnetic field by the discharge and Hall currents are not considered.

The HiPIMS discharge was fed by a HiPIMS generator model SPIK2000A by Melec GmbH capable of delivering pulses up to 1 kV, up to 500 A, with freely adjustable duration greater than 5 μs and a repetition rate of up to 50 kHz. A Pinnacle DC power supply (maximum 1 kV, maximum 5 kW, manufactured by Advanced Energy) was used to charge the capacitors of the SPIK2000A pulser. The pulser was operated in unipolar negative mode with typical HiPIMS parameters which were kept the same throughout the experiments: The voltage on-time was set to 100 μs with a pulse repetition rate of 100 Hz. This resulted in a peak current of about 170 A and an average power of 240 W. The nominal peak power density, averaged over the target area, reached 1.8×10^7 W/m². No power was applied to the target during the off-time between pulses. The anode was always grounded. All signals were recorded using ground as the reference potential.

The discharge current was inductively picked up using a current transformer (Pearson model 101, sensitivity 0.01 V/A, 3-dB bandwidth 0.25 Hz - 4 MHz). The discharge voltage was recorded at the power feedthrough to the target using a 100× high voltage probe (Tektronix P5100, 100 MΩ input impedance, 3-dB 250 MHz bandwidth). All electrical signals were recorded with a National Instruments PXI-5105 high speed digitizer/oscilloscope with up to 60 MS/s real-time sampling rate per channel, operated under a LabView SignalExpress program.

To reduce electromagnetic interference, the output of the SPIK pulse generator was fed through a common-mode filter consisting of three ferrite rings. The need to filter is primarily due to the long, unshielded cables that are used to connect the pulse generator to the magnetron. Unfiltered connections like these can easily experience voltage shifts above ground (common noise), which induce measurement error when measuring with respect to ground. This is especially true in pulsed power systems, where $L\cdot di/dt$ transients, as well as conducted and radiated noise, are prevalent.

The emissive probe was aligned in the axial direction, as indicated in Fig. 1, and radially scanned from r = 0 mm up to r = 38 mm from the center in Δr = 1 mm steps using a computer-controlled stepper motor synchronized with the data acquisition system. Then, the axial position of the magnetron was changed and the next radial scan of the probe executed without having to

break vacuum. The axial positions covered the range from z = 1 mm near the target to z = 72 mm relatively far away from it. The measurements locations are depicted by the position of the grid points in Fig. 1. The step size was set to Δz = 1 mm in the range 1 mm $\leq z \leq$ 20 mm, and increased to Δz = 2 mm in the range 20 mm $\leq z \leq$ 40 mm, and to Δz = 4 mm in the range 40 mm $\leq z \leq$ 72 mm, thereby defining a measurement grid of 39 × 38 = 1482 locations. The such-defined region covers most of the target pre-sheath and includes a typical substrate position. Positions near the racetrack, however, could not be measured since the physical presence of the probe excessively disturbed the plasma. The closest distance of the probe to the racetrack was 15 mm. As the probe nears the racetrack, ignition of the HiPIMS pulses was hindered, presumably because the probe intersected magnetic field lines that guided a crucial portion of the magnetized plasma electrons. It appears that the presence of the probe interferes with the closed drift (Hall) current and causes a large decrease in the discharge current. The lack of data near the racetrack will be visible when the results are presented in graphical form.

The emissive probe used for this experiment was made of tungsten wire with a diameter of 75 μm that forms a 1.5 mm diameter semi-circle loop. The loop was push-fitted into the holes of a 140 mm long double-bore alumina ceramic tube with an outer diameter of 1.57 mm and inner bore diameters of 0.41 mm each. The plane of the probe loop was aligned parallel to the magnetic field lines to reduce the disturbing effect of the probe. The wire loop geometry turned out to be less intrusive than the coil-filament probe described in our pulsed probe paper.[43] Inside the bores the tungsten wire was spliced with thin, 50-μm diameter copper threads to increase conductivity and reduce ohmic losses. This ensures that only the exposed probe loop glows when the heating current is applied. The cold-state resistance between the two probe connectors was 0.78 Ω, increasing to 1.91 Ω when heated to operational temperature. Ohmic heating of the probe wire was achieved by a pulsed current gated out of phase with the HiPIMS discharge pulse as explained in our previous work.[43] The pulsed nature of the heating cycles enabled the use of a 1:1 isolation transformer to couple the heating current from a grounded power supply to the floating probe. The potential of the floating emissive probe was measured using an attenuating (100×) voltage probe (Tektronix P5100) connected to the NI PXI 5105 data acquisition system (*cf*. Fig. 1). A TTL pulse generator (TENMA TGP110) synchronized the experiment; it gated the heating pulse as well as a delay generator (Tektronix PG508) that was connected to the external gate input of the SPIK2000A pulser.

A cold cylindrical Langmuir probe was used in order to measure the cold-probe floating potential as a comparison to plasma potential measurements using the emissive probe. The probe was constructed of 75 μm diameter tungsten wire, where a 3 mm long tip segment was exposed to the plasma. The rest of the probe wire was surrounded by a 0.5 mm diameter, 140 mm long ceramic tube. This probe is more robust than a filament probe and its lateral extension is smaller than the emissive probe, hence our preference to use the cylindrical probe for cold-probe floating potential measurements.

The radial position of the probe (cold or emissive) was again set by LabView SignalExpress software by controlling a linear motion feedthrough system with stepper motor. The software synchronized probe positioning and potential data acquisition. Data analysis and visualization was carried out using custom MATLAB scripts.

IV. RESULTS

A. Magnetic field measurements

Figure 2 (top) shows the measured magnetic field distribution in the *r*-*z* plane. The vector arrows indicate the direction of the magnetic field **B**, while the contour plot shows the magnitude of $|\mathbf{B}| = \left(B_r^2 + B_z^2\right)^{1/2}$. This measurement would represent the entire information for the discharge volume if perfect axial symmetry of the magnetron were applicable. However, as Fig. 2 shows, there are notable deviations from symmetry.

The field lines arching from the outer ring magnet to the central magnet show the extent of the magnetic pre-sheath where electrons are confined and experience closed $\mathbf{E} \times \mathbf{B}$ drift. The location of the highest sputter erosion, the racetrack, can be found where the magnetic field lines are about parallel to the target surface. This is the case for radii in the range 16 mm < r < 28 mm. The magnetic null was found at z = 44 mm from the surface of the target slightly off the center line. A magnetic null point so close to the target is indicative for a very unbalanced magnetron,[44] which is confirmed by the presence of field lines guiding plasma away from the magnetron.

B. Emissive probe parameters

The next step of the experiment focused on correct timing of filament heating and magnetron discharge pulses and ensuring that the electron emission during HiPIMS pulses is sufficient. Fig. 3 shows the waveforms for the probe's heating voltage pulse V_{fil} with the associated filament heating current I_{fil}, the emitted electron current I_{em}, and the gate pulse V_{gate} for one HiPIMS pulse. A 6 V pulse is applied to the tungsten filament to heat it. At 2.1 ms, heating is terminated, followed by a delay of 350 μs before the HiPIMS target voltage is applied. The electron emission current decays relatively slowly, which ensures that electron emission is practically constant during the HiPIMS pulse, as depicted in the inset of Fig. 3. The electron emission current drops from 2.115 mA to 2.080 mA during the HiPIMS pulse on-time, corresponding to a change of only 1.6%.

In order to ensure that the emitted electron current is sufficient, one can look for the change of the probe's floating potential as the electron emission current is increased, *cf*. Eq. (3). Figure 4 shows the measured floating potential as a function of the heating current for two different measurement locations. The graph is composed of many data points, each of them recorded using a different HiPIMS pulse but at nominally identical discharge conditions. When the probe was cold or insufficiently heated, the floating potential was about -17.5 V or respectively -47 V, depending on position. The floating potential increased when the heating current reached 1.0 A. The probe potential saturated at about -13.5 V or -30 V, respectively. A relatively high heating current of 2.6 A was chosen for all experiments thereby ensuring that the emissive probe works in the saturation regime and the emissive probe potential is approximately equal to the plasma potential.

C. Potential measurements

The time evolution of discharge current $I_d(t)$, plasma potential $V_p(t)$ as measured with the hot probe, and floating potential $V_f(t)$ as measured with the cold probe, all averaged over 100 pulses, are displayed in Fig. 5 for the location r = 24 mm, z = 22 mm. The shaded areas around the average curves are the envelopes including the data of all 100 pulses. The reference time $t = 0$ was defined at the time when the discharge current shows a distinct onset in a semi-logarithmic plot as depicted in the inset of Fig. 5, as opposed to the time when the voltage is applied to the target. This kind of $t = 0$ definition was adopted in order to eliminate the issues associated with the jitter caused by the statistical time delay[45] of the measurable discharge current onset. This approach allowed us to meaningfully average the measured signals of currents and voltages using 100 discharge pulses per location. The applied discharge voltage (target potential relative to the grounded anode) was always -488 V and therefore will not be further displayed or discussed; this voltage was constant for the entire pulse duration due to the very large energy-storing capacitance of the SPIK2000A pulse power supply.

The discharge current pulse has approximately a triangular shape with a peak current of 170 A. The triangular shape indicates that the current has not reached the maximum that could develop for the given applied voltage if the pulse duration were longer. In that sense, we deal with short-pulse HiPIMS.

The floating potential of probes is very sensitive to the balance of charged particles arriving at and leaving the probe. As shown in Fig. 5, the plasma potential waveform shows a rapid drop to negative values at the initial stage of the discharge even well before the Pearson current transformer reads discharge current.

In order to obtain the electric field one needs plasma potential measurements at as many locations as possible. Since we measure only at one location at a time, it made sense to determine representative potential values for the location at a function of time, which led us to collect data from 100 individual pulses and produce an average as indicated in Fig. 6. However, we should not disregard the information carried provided by individual pulses. Figure 6 shows therefore plasma potential measurements that were not averaged. One can discern oscillations on a microsecond time scale. They are not measurement noise but potential oscillations which are associated with traveling dense plasma zones and plasma protuberances.[18]

D. Evolution of the plasma potential and related electric field

The array of graphs in Fig. 7 shows the temporal and spatial evolution of the plasma potential distribution measured by the emissive probe based on averaging 100 pulses per location. Individual oscillations and fluctuations are smoothed in this way, and one should keep in mind that individual events can exhibit strong transient deviations. Once the electric potentials are known one can derive the corresponding electric field according to

$$\mathbf{E} = -\nabla V_p \qquad (4)$$

which is also included in Fig. 7. For better visualization of the measured data, potential distributions $V_p(r,z)\big|_t$ in the (r,z) plane were determined at selected times by linearly interpolating between the data points. The dynamics of the plasma potential distribution is best seen in a video clip showing the evolution of the $V_p(r,z)\big|_t$ surfaces, which can be found in the on-line *auxiliary material*.

E. Evolution of the cold-probe floating potential

While plasma potential measurements are at the center of this work, it is also interesting to consider the evolution of the floating potential determined by a cold, non-emitting probe. The difference between plasma potential and cold-probe floating potential gives clues on the electron energy or electron temperature if the electrons were Maxwell-distributed. At a distance of about 4 cm from the target surface, the difference is 4 V (Fig. 4), leading to an electron temperature of about 1 eV using $e(V_p - V_f)/T_e \approx \ln(m_e/m_i)/2$ (where V_f is here the cold probe floating potential and T_e is in eV; see e.g. ref.[25]).

Fig. 8 shows the result that was obtained in analogous way to Fig. 7 but without probe heating. Not unexpectedly, we see similar general features: most strikingly large negative potentials with respect to the grounded anode in the magnetic pre-sheath.

F. Distribution of the electrons' Hall velocity

The distribution of the electron drift velocity $\mathbf{E}\times\mathbf{B}/B^2$ can be found based on the knowledge of the derived electric field $\mathbf{E} = -\nabla V_p$ and the measured static magnetic field **B**. The change of the magnetic field due to the Hall current and discharge current is neglected in this consideration. As mentioned before, only electrons are subject to the drift since ions are too heavy and thus their gyration radius is larger than the system's characteristic size. Using the data from Fig. 2 for the static magnetic field and the various **E**-field distributions as determined from the plasma potential, the corresponding drift velocities can be derived as shown in Fig. 9. The positive values of the drift velocities belong to vectors pointing into the (r,z) plane. Since the electric field data were derived from averages of 100 measurements for each of probe locations, the velocity results are representative in an average sense. The actual local field could temporarily be much different and so would be the actual electron drift velocity.

V. DISCUSSION

The electric field between cathode and anode is highly non-uniform before and even more-so during the HiPIMS discharge. Once the discharge plasma is established, most of the anode-cathode voltage drop, which is typically several hundred volts, is concentrated in the space-charge layer, known as the sheath, right adjacent to the target surface.

Although the Child formula for the sheath thickness is not directly applicable due to the presence of a magnetic field and non-Maxwellian electrons, it can be used for an order-of-magnitude estimate,

$$s_{Child} = \frac{\sqrt{2}}{3}\lambda_{De}\left(\frac{2eV_0}{kT_e}\right)^{3/4}, \tag{5}$$

where λ_{De} is the Debye length:

$$\lambda_{De} = \left(\frac{\varepsilon_0 kT_e}{n_e e^2}\right)^{1/2}. \tag{6}$$

For an order of magnitude estimate we use $kT_e \sim 1\,\mathrm{eV}$, $n_e \sim 10^{19}\ \mathrm{m}^{-3}$, and $V_0 = 600\ \mathrm{V}$ as the applied voltage, and we find $\lambda_{De} \sim 10^{-5}\,\mathrm{m}$ and $s_{Child} \sim 10^{-3}\,\mathrm{m}$. The zone adjacent to the sheath, the magnetic pre-sheath, accommodates an important portion of the voltage drop, of order of 10-20% of the total discharge voltage, which is the subject of the measurements presented here. While this is generally well known for magnetron sputtering, the here-presented data give details on the spatial and temporal distribution of the potential for the conditions of HiPIMS discharges.

We deal with a highly unbalanced magnetron characterized by a magnetic zero point only 43 mm from the target surface (Fig. 2). In the region beyond this point, $z > 43$ mm near axis and at even smaller distances z at large radii r, the magnetic field lines guide plasma away from the magnetron. In those regions relatively distant from the target surface, the magnetic field is weak and the plasma potential reveals only small spatial and temporal variations, hence the electric field is weak. This is expected since plasma exhibits one plasma potential in the limiting case when the external magnetic field is absent.

From Fig. 5 we see that soon after the application of the voltage pulse, the plasma and floating potentials shift negatively before the detectable onset of the discharge current (see definition of $t = 0$ in the inset of Fig. 5). This indicates that a weak plasma is already present and developing at an early stage, before $t = 0$, in agreement with previous considerations of plasma onset.[45]

A shift to negative plasma potential (Fig. 7) can be explained by the removal of ions — due to acceleration in the electric field— leaving behind the confined, drifting and accumulating electrons. One of the important results from Fig. 7 is the striking 3-dimensional character of the electric field accelerating ions toward the racetrack. The electric field is like a funnel that guides and concentrates the ions. This leads to a concentration of power density in the racetrack. One can infer many consequences such as a high and non-uniform temperature enhancement of the target surface, possibly causing sublimation (for materials of high vapor pressure) and affecting the yields of sputtering and secondary electron emission. It is clear that the racetrack region is thus comprised of both a high neutral density and a high plasma density. The concentration also indicates that the generally quoted power densities for HIPIMS, averaged over the target area, are really just nominal values, with the physically relevant power density greatly exceeding the nominal power density.

Another interesting finding from Fig. 7 is the establishment of a highly non-uniform and occasionally non-monotonic, asymmetric potential profile. It exhibits a small maximum at certain times and locations (for example, Fig. 7, t = 17 μs, r = 30 mm, z = 30 mm) with a steep slope to the target and a very shallow slope to the substrate. Ions on the target side of a maximum are accelerated to the target, causing sputtering and secondary electron emission, and ions on the substrate side can escape. The existence of such profile, albeit with less features and detail, was inferred from ion energy measurements at different distances from the target.[46]

One can come to similar conclusions using the measurements of the cold-probe floating potential due to the generally similar behavior of plasma and floating potentials. Figure 8 shows the funnel shape of the cold-probe floating potential distribution. While the electric field is based on the gradient of the plasma potential, it can be useful to consider the distribution of the cold-probe floating potential, which is easier to acquire because it does not require any probe heating and one does not worry about the emission current.

In this context we refer to our preliminary data, reproduced here as Fig. 10, which were presented at a recent conference.[47] This figure illustrates a situation where the emissive probe filament does not emit a sufficient electron current to satisfy the condition $I_{em} \geq I_{es} - I_{is}$ over all space. In certain regions, the emissive probe floating potential approximately assumed the plasma potential, as desired, since the electron emission was sufficient. However, in other regions, the probe's floating potential was closer to the floating potential of a cold probe. This caused the appearance of a strange valley, in a dense plasma region, which was identified as an artifact by increasing the heating of the probe. The wall height of the valley, typically about 10 V, can be used as a measure for the electron temperature, or more generally the electron energy, as mentioned before.

With the knowledge of the electric and magnetic fields, the electrons' closed drift velocity was determined as shown in Fig. 9. We see (i) the drift velocities are of order of 10^5 m/s and (ii) there are very strong variations depending on the local fields. The latter is quite surprising since the data were derived from averaging over 100 pulses per location. The former finding is very relevant in the context of a companion paper on fast imaging HiPIMS discharges, where it was shown that the plasma density is highly localized in the azimuthal direction of this planar magnetron.[18] The formation of such dense plasma structures was explained by the difference of electron drift velocity (10^5 m/s) and the traveling velocity of the dense plasma structure (10^4 m/s). Roughly speaking, the energetic electrons freely reach the dense plasma zones where the interactions are much stronger and where it is very likely that they cause several ionizing collisions, thereby amplifying the dense plasma structures.[18]

It is unfortunate that the probe technique can only record a *local* potential as a function of time, as opposed to simultaneously measuring the entire field of potentials. To obtain plasma potential at many places and derive the electric field, the measurements involved moving the probe and using many (here about 10^6) HiPIMS pulses. Since the plasma structures drift azimuthally, the properties should be smeared out at least in the azimuthal direction. The fact that the averaged probe data show very pronounced structures indicate that initial fluctuations and amplifications are not random but perhaps triggered by small asymmetries of the magnetron, i.e. the structures seem to develop with some statistical regularity as opposed to being random.

In ref.[18] it was suggested that the region of strongest azimuthal density gradient is necessarily related to an azimuthal electric field, which gives rise to a localized $\mathbf{E}_\theta \times \mathbf{B}$ drift, which is in the direction of the *z*-axis. Here, the pulse-averaged potential data suggest that the electric field varies a lot depending on location and time into the pulse. There are even regions where the electric field points to the substrate, giving rise to ion acceleration away from the target. In the animated sequence of the plasma potential distribution one can see a wave propagating away from the target with a velocity of about 1800 m/s. The origin of this wave is not obvious given that we deal with data averaged over many pulses and that a complicated field structure is present. It is interesting to consider this wave as an ion-acoustic wave and apply the approximate formula for the ion sound speed (which is strictly speaking only valid in the absence of a magnetic field and for $T_i < T_e$),

$$v_s \approx \left(\frac{kT_e}{m_i} \right)^{1/2} . \qquad (7)$$

Using the mass of niobium ions and the measured velocity, Eq. (7) leads to an electron temperature of 3 eV, a reasonable value.

The structures found in the electric field translate into structures in the Hall velocities. For example, when the discharge current sharply rises, at $t = 4$ μs, "islands" of reverse velocity form. This, again, indicates that the moving dense plasma structures seen in ref.[18] are not fully random but develop more or less regularly as the discharge pulses evolve.

SUMMARY AND CONCLUSIONS

The evolution of the plasma potential distribution of HiPIMS discharge has been mapped using a pulse-heated emissive probe. To keep the data manageable, the discharge parameter were kept constant: Nb target of 75 mm diameter in argon at 0.26 Pa, 100 μs constant voltage pulses, 100 Hz, resulting in peak current of 170 A and an average power of 240 W. The probe positioning and data collection were automated, with 100 pulses recorded for each position. The time-dependent plasma potential distributions are presented in figures and as an animated movie available on-line.

It was found that the plasma potential drops towards the target, resulting in an electric field that accelerates ions toward the target. About 10-20% of the total applied voltage drops in the magnetic presheath, which is determined by the magnetic field structure and extends about 40 mm in the case of our unbalanced magnetron. The rest of the voltage drops in the target sheath and very little in the plasma extending beyond the presheath. The sheath and the immediately adjacent presheath region near the racetrack were not accessible to probe measurements due the very large disturbance of the discharge by the presence of the probe.

The plasma potential shifts negatively soon after application of the voltage pulse and before one can discern a discharge current as measured by the Pearson current detector. This indicates the presence of charge particles and evolution plasma at early times, which is in agreement with observations in the literature that the onset of a current pulse depends on the presence of plasma, the pulse repetition rate and other factors.

Despite averaging over 100 pulses per position, the plasma potential data show systematic variations. Occasionally one finds a local reversal of the electric field, affecting the $\mathbf{E}\times\mathbf{B}$ electron drift. The $\mathbf{E}\times\mathbf{B}$ electron drift velocity was found to be of order of 10^5 m/s, which is important in light of other recent results showing the existence of dense plasma zones over the racetrack traveling with typically 10^4 m/s. The difference of electron drift velocity and the speed of dense plasma zones is important for the formation mechanism of the traveling plasma structures.

ACKNOWLEDGMENTS

We thank J. Wallig for technical support. A.R. thanks the Austrian Marshall Plan Foundation (www.marshallplan.at) for funding a scholarship. A.A. acknowledges support by the Assistant Secretary for Energy Efficiency and Renewable Energy, Office of Building Technology of the U.S. Department of Energy. This work was done at Lawrence Berkeley National Laboratory with support by the U.S. Department of Energy under Contract No. DE-AC02-05CH11231.

References

[1] A. Ehiasarian, in *Plasma Surface Engineering Research and its Practical Applications*, edited by R. Wei (Research Signpost, Kerala, India, 2008), p. 35.
[2] K. Sarakinos, J. Alami, and S. Konstantinidis, Surf. Coat. Technol. **204,** 1661 (2010).
[3] J. T. Gudmundsson, Vacuum **84,** 1360 (2010).
[4] U. Helmersson, M. Lattemann, J. Bohlmark, A. P. Ehiasarian, and J. T. Gudmundsson, Thin Solid Films **513,** 1 (2006).
[5] A. Hecimovic and A. P. Ehiasarian, J. Appl. Phys. **108,** 063301 (2010).
[6] A. Anders, Thin Solid Films **518,** 4087 (2010).
[7] J. Bohlmark, J. T. Gudmundsson, J. Alami, M. Lattemann, and U. Helmersson, IEEE Trans. Plasma Sci. **33,** 346 (2005).
[8] J. Alami, J. T. Gudmundsson, J. Bohlmark, J. Birch, and U. Helmersson, Plasma Sources Sci. Technol. **14,** 525 (2005).
[9] A. P. Ehiasarian, R. New, W.-D. Münz, L. Hultman, U. Helmersson, and V. Kouznetsov, Vacuum **65,** 147 (2002).
[10] J. Bohlmark, M. Lattemann, J. T. Gudmundsson, A. P. Ehiasarian, Y. Aranda Gonzalvo, N. Brenning, and U. Helmersson, Thin Solid Films **515,** 1522 (2006).
[11] A. Anders, J. Andersson, and A. Ehiasarian, J. Appl. Phys. **102,** 113303 (2007).
[12] A. Anders, Surf. Coat. Technol. **205,** S1 (2011).
[13] A. Anders, J. Čapek, M. Hála, and L. Martinu, J. Phys D: Appl. Phys. **45,** 012003 (2012).
[14] S. M. Rossnagel and H. R. Kaufman, J. Vac. Sci. Technol. A **5,** 88 (1987).
[15] J. Bohlmark, U. Helmersson, M. VanZeeland, I. Axnäs, J. Alami, and N. Brenning, Plasma Sources Sci. Technol. **13,** 654 (2004).
[16] D. Lundin, U. Helmersson, S. Kirkpatrick, S. Rohde, and N. Brenning, Plasma Sources Sci. Technol. **17,** 025007 (2008).
[17] A. F. Alexandrov, L. S. Bogdankevich, and A. A. Rukhadze, *Principles of Plasma Electrodynamics* (Springer, Berlin, 1984).
[18] A. Anders, P. Ni, and A. Rauch, J. Appl. Phys.**,** submitted for review (2012).
[19] A. Vetushka, S. K. Karkari, and J. W. Bradley, J. Vac. Sci. Technol. A **22,** 2459 (2004).
[20] A. Mishra, G. Clarke, P. Kelly, and J. W. Bradley, Plasma Processes and Polymers **6,** S610 (2009).
[21] A. Mishra, P. J. Kelly, and J. W. Bradley, Plasma Sources Sci. Technol. **19,** 045014 (2010).
[22] A. Hecimovic and A. P. Ehiasarian, J. Phys. D: Appl. Phys. **42** (2009).
[23] P. Poolcharuansin and J. W. Bradley, Plasma Sources Sci. Technol. **19,** 025010 (2010).
[24] P. M. Chung, L. Talbot, and K. J. Touryan, *Electric Probes in Stationary and Flowing Plasmas: Theory and Applications* (Springer, Berlin, 1975).
[25] I. H. Hutchinson, *Principles of Plasma Diagnostics* (Cambridge University Press, Cambridge, UK, 2002).
[26] J. W. Bradley, S. Thompson, and Y. A. Gonzalvo, Plasma Sources Sci. Technol. **10,** 490 (2001).
[27] J. W. Bradley, S. K. Karkari, and A. Vetushka, Plasma Sources Sci. Technol. **13,** 189 (2004).
[28] N. Hershkowitz, B. Nelson, J. Pew, and D. Gates, Rev. Sci. Instrum. **54,** 29 (1983).
[29] S. Iizuka and et al., J. Phys. E: Sci. Instrum. **14,** 1291 (1981).
[30] R. F. Kemp and J. J. M. Sellen, Rev. Sci. Instrum. **37,** 455 (1966).
[31] N. Mahdizadeh and et al., Plasma Physics and Controlled Fusion **47,** 569 (2005).

[32] I. Picková, A. Marek, M. Tichý, P. Kudrna, and R. Apetrei, Czechoslovak Journal of Physics **56,** B1002 (2006).
[33] J. R. Smith, N. Hershkowitz, and P. Coakley, Rev. Sci. Instrum. **50,** 210 (1979).
[34] E. Y. Wang, T. Intrator, and N. Hershkowitz, Rev. Sci. Instrum. **56,** 519 (1985).
[35] J. P. Sheehan, Y. Raitses, N. Hershkowitz, I. Kaganovich, and N. J. Fisch, Phys. Plasmas **18,** 073501 (2011).
[36] A. Anders, *Cathodic Arcs: From Fractal Spots to Energetic Condensation* (Springer, New York, 2008).
[37] *Smithells Metals Reference Book*, edited by W. F. Gale and T. C. Totemeier (Elsevier, Amsterdam, 2004).
[38] P. Balan, R. Schrittwieser, C. Ionita, J. A. Cabral, H. F. C. Figueiredo, H. Fernandes, C. Varandas, J. Adamek, M. Hron, J. Stockel, E. Martines, M. Tichy, and G. Van Oost, Rev. Sci. Instrum. **74,** 1583 (2003).
[39] G. D. Hobbs and J. A. Wesson, Plasma Physics **9,** 85 (1967).
[40] N. Hershkowitz, IEEE Trans. Plasma Sci. **22,** 11 (1994).
[41] J. W. Bradley, R. A. Khamis, M. I. Sanduk, J. A. Elliott, and M. G. Rusbridge, J. Phys D: Appl. Phys. **25,** 1443 (1992).
[42] E. Mravlag and P. Krumm, Rev. Sci. Instrum. **61,** 2164 (1990).
[43] J. Sanders, A. Rauch, R. Mendelsberg, and A. Anders, Rev. Sci. Instrum. **82,** 093505 (2011).
[44] I. V. Svadkovski, D. A. Golosov, and S. M. Zavatskiy, Vacuum **68,** 283 (2002).
[45] G. Y. Yushkov and A. Anders, IEEE Trans. Plasma Sci. **38,** 3028 (2010).
[46] D. Horwat and A. Anders, Appl. Phys. Lett. **97,** 221501 (2010).
[47] A. Rauch, J. M. Sanders, R. Mendelsberg, and A. Anders, in *2nd Int. Conf. on HIPIMS* (Braunschweig, Germany, 2011).

Figure Captions

FIG. 1. Experimental setup showing the arrangement and basic circuitry of the magnetron and probe diagnostics.

FIG. 2. Measured magnetic field and field line directions for the magnetron used; top: |B| on a axial line above the racetrack at r = 24 mm, and right: |B| in radial direction at z =1 mm.

FIG. 3. Waveforms for the probe's heating voltage pulse, V_{fil}, with the associated filament heating current, I_{fil}, the emitted electron current, I_{em}, and the gate pulse, V_{gate}, for one HiPIMS pulse.

FIG. 4. Floating potential as a function of the heating current, at the probe positions (r = 28 mm, z = 20mm) and (r = 28 mm, z = 40mm). The floating potential approaches to the plasma potential when the heating current exceeds about 2.1 A.

FIG. 5. Plasma and floating potential waveforms, averaged over 100 pulses, measured at the probe position (r = 24 mm, z = 22 mm). Additionally, the discharge current waveform is shown or an applied voltage of 488 V, pulse width 100 μs, at a repetition rate of 100 Hz leading to peak current 170 A. The shaded areas around the averaged pulse shapes represent the envelopes containing data of all 100 pulses.

FIG. 6 Non-averaged plasma potentials measured at (r = 20 mm, z = 15 mm). The black curve is one example showing relatively large amplitude oscillations corresponding to frequencies in the range 20-100 kHz; the thin-line curves (red in the on-line version) are overlaid to illustrate the construction of the grey envelopes shown in Fig. 5; the central (blue in the on-line version) curve is the arithmetic mean of 100 pulses.

FIG. 7(a) and (b). Distribution of plasma potential (left column) and derived electric field (right column) at different times during a HiPIMS pulse. Each data point is the mean of 100 individual measurements. Fig.7(b) is a continuation of Fig. 7(a).

FIG. 8. Floating potential distributions for selected times during a HiPIMS pulse.

FIG. 9. Distribution of the electron $\left|\mathbf{E}\times\mathbf{B}/B^2\right|$ velocities, where **B** is the static field originating from the permanent magnetics and the **E** field is derived from the measured plasma potential averaged over 100 pulses. In this sense, the velocity distributions displayed are smoothed and the actual and instantaneous drift velocities deviate from this average. The subfigures correspond to the beginning, middle and end of HiPIMS pulses. Positive values for the velocity imply a velocity vector direction into the (r,z) plane.

FIG. 10. Plasma potential distribution 4 μs after current onset ($t = 0$) as recorded using a hot probe whose emission current is not sufficiently high everywhere; this results in a valley region where the probe's floating potential indicates a cold probe's potential rather than the hot probe potential (*cf*. Fig. 4).

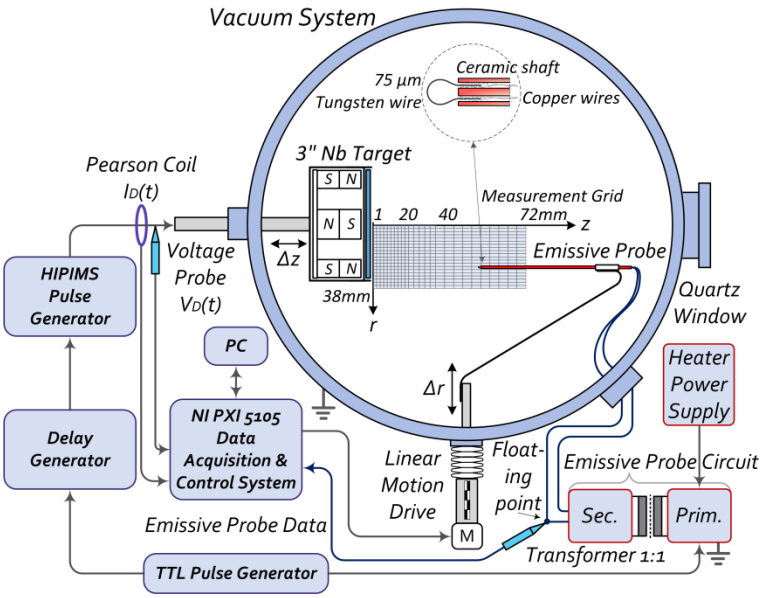
Vacuum System
75 µm
Tungsten wire
Ceramic shaft
Copper wires
3" Nb Target
Pearson Coil
$I_D(t)$
Measurement Grid
72mm
z
1 20 40
Δz
Voltage
Probe
$V_D(t)$
Emissive Probe
HIPIMS
Pulse
Generator
38mm
r
Quartz
Window
PC
Heater
Power
Supply
Δr
Delay
Generator
NI PXI 5105
Data
Acquisition &
Control System
Linear
Motion
Drive
Float-
ing
point
Emissive Probe Circuit
Sec.
Prim.
M
Emissive Probe Data
Transformer 1:1
TTL Pulse Generator

FIG. 1

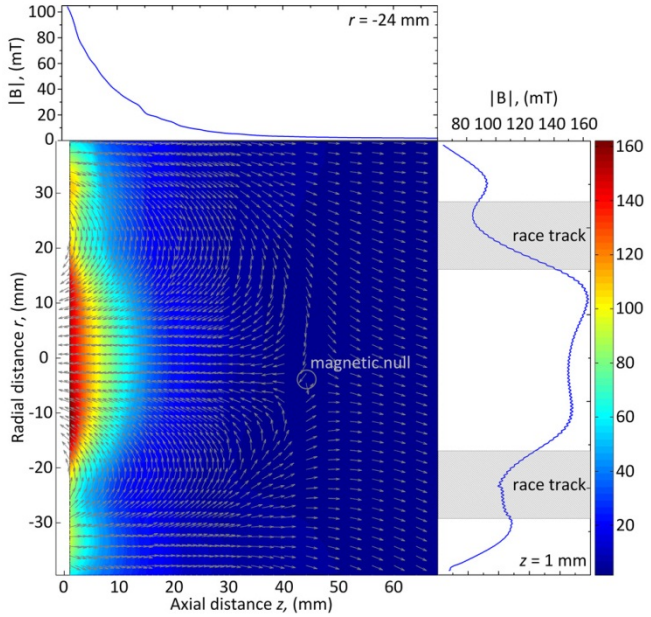
r = -24 mm
|B|, (mT)
|B|, (mT)
80 100 120 140 160
race track
race track
magnetic null
z = 1 mm
Radial distance r, (mm)
Axial distance z, (mm)

FIG. 2

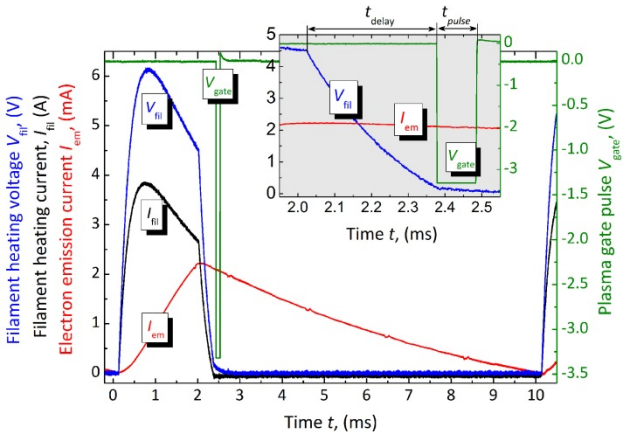
t_{delay}
t_{pulse}
V_{fil}
I_{fil}
I_{em}
V_{gate}
Filament heating voltage V_{fil}, (V)
Filament heating current, I_{fil} (A)
Electron emission current I_{em}, (mA)
Plasma gate pulse V_{gate}, (V)
Time t, (ms)
Time t, (ms)

FIG. 3

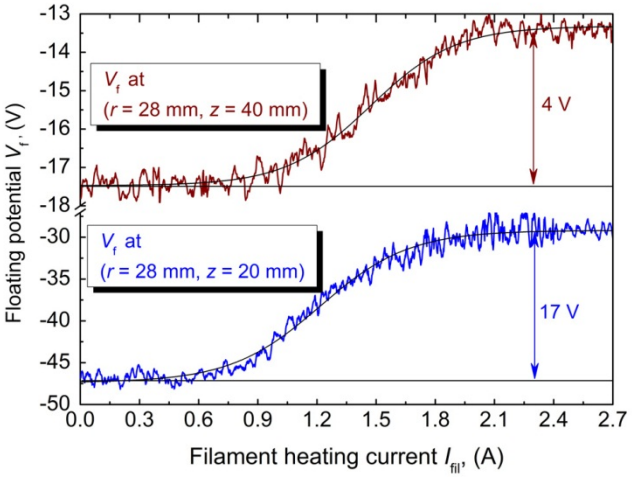
-13
-14
-15
-16
-17
-18
-30
-35
-40
-45
-50
0.0
0.3
0.6
0.9
1.2
1.5
1.8
2.1
2.4
2.7
Floating potential V_f, (V)
Filament heating current I_{fil}, (A)
V_f at
(r = 28 mm, z = 40 mm)
4 V
V_f at
(r = 28 mm, z = 20 mm)
17 V

FIG. 4

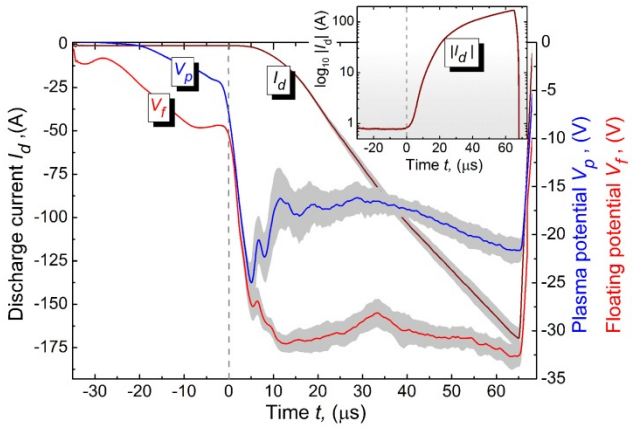
Discharge current I_d,(A)
Plasma potential V_p, (V)
Floating potential V_f, (V)
Time t, (μs)
V_p
V_f
I_d
$\log_{10}|I_d|$ (A)
$|I_d|$
Time t, (μs)

FIG. 5

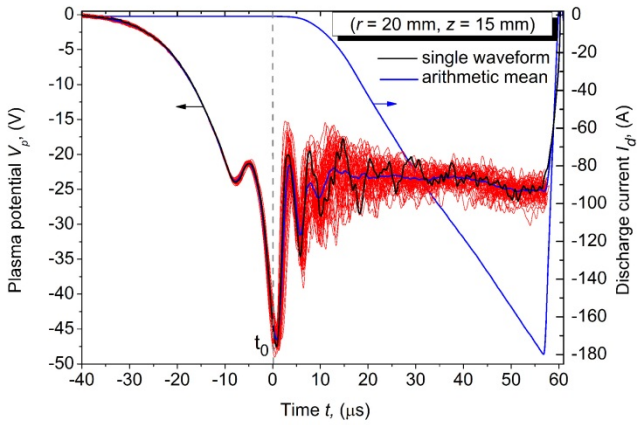
(r = 20 mm, z = 15 mm)
single waveform
arithmetic mean
Plasma potential V_p, (V)
Discharge current I_d, (A)
Time t, (μs)
t_0

FIG. 6

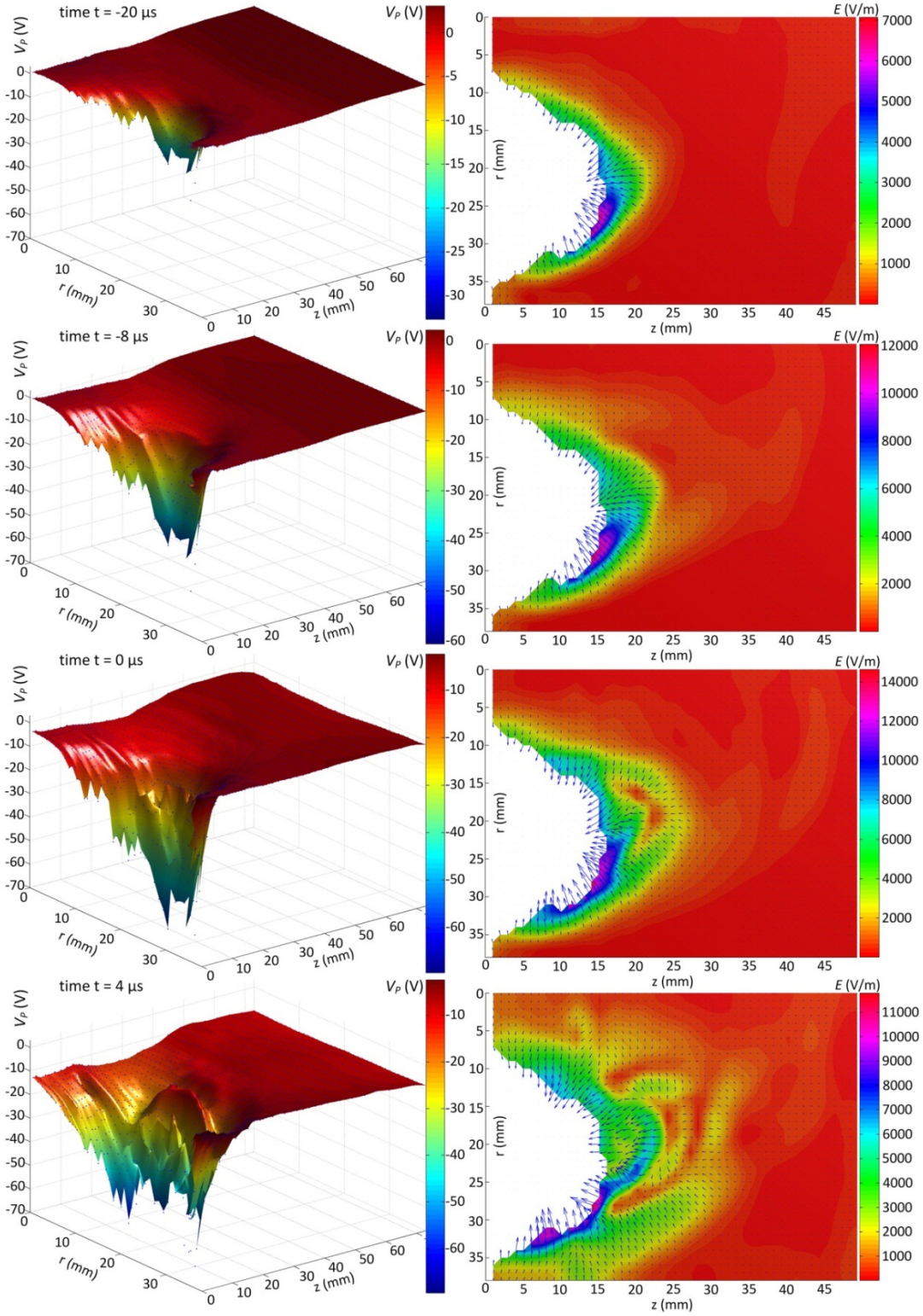

FIG. 7(a)

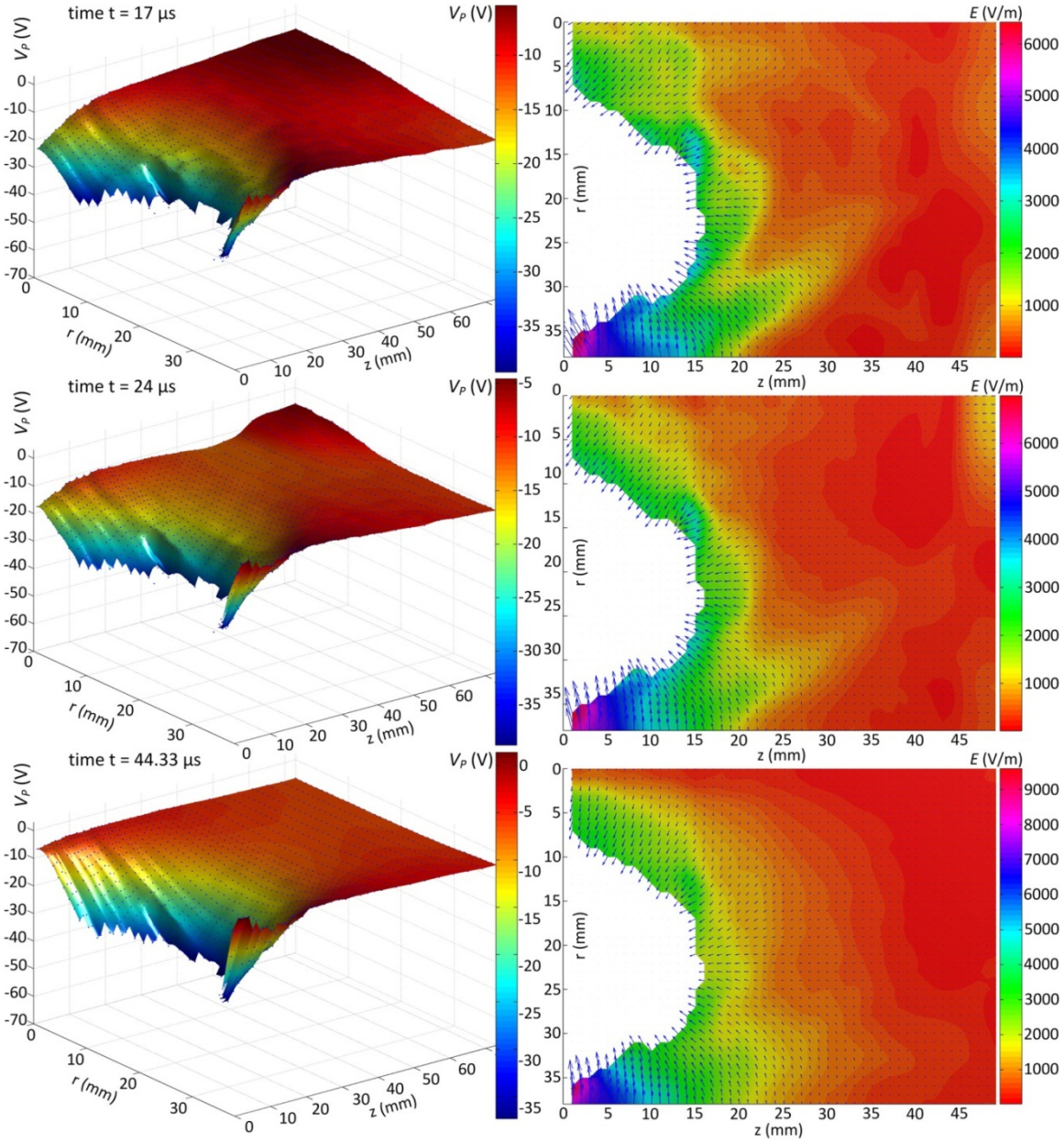

FIG. 7(b)

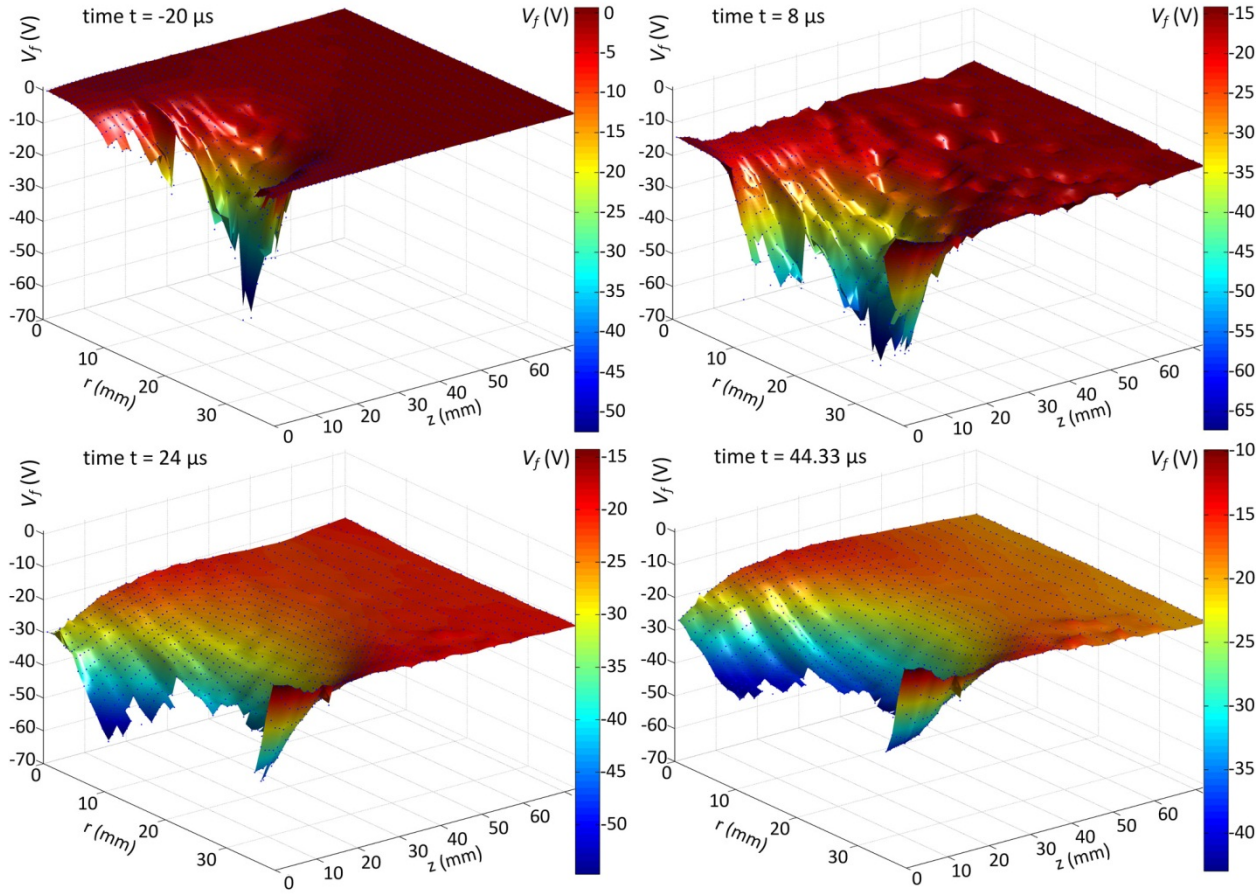

FIG. 8

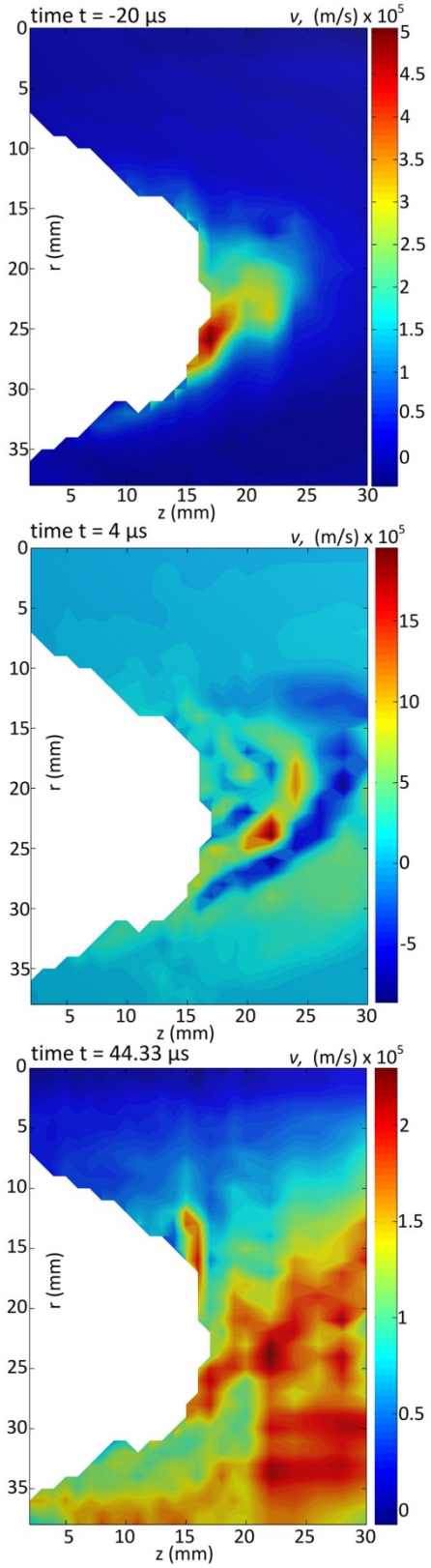
time t = -20 µs
v, (m/s) x 10^5
r (mm)
z (mm)
time t = 4 µs
v, (m/s) x 10^5
r (mm)
z (mm)
time t = 44.33 µs
v, (m/s) x 10^5
r (mm)
z (mm)

FIG. 9

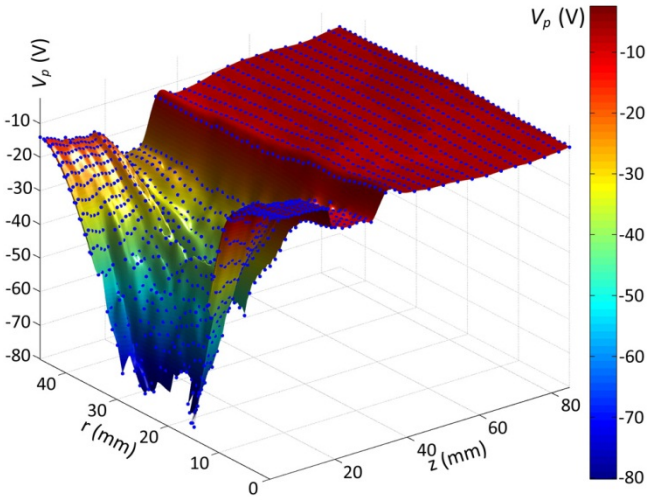
V_p (V)
-10
-20
-30
-40
-50
-60
-70
-80
40
30
20
10
0
r (mm)
20
40
60
80
z (mm)
V_p (V)
-10
-20
-30
-40
-50
-60
-70
-80

FIG. 10